Supplementary Information: Anomalous continuum scattering and higher-order van Hove singularity in the strongly anisotropic *S* = 1/2 triangular lattice antiferromagnet

Pyeongjae Park[1*], E. A. Ghioldi[2], Andrew F. May[1], James A. Kolopus[1], Andrey A. Podlesnyak[3], Stuart Calder[3], Joseph A. M. Paddison[1], A. E. Trumper[4], L. O. Manuel[4], Cristian D. Batista[2,5], Matthew B. Stone[3*], Gábor B. Halász[1*] & Andrew D. Christianson[1*]

[1]*Materials Science and Technology Division, Oak Ridge National Laboratory, Oak Ridge, Tennessee 37831, USA*
[2]*Department of Physics and Astronomy, University of Tennessee, Knoxville, Tennessee 37996, USA*
[3]*Neutron Scattering Division, Oak Ridge National Laboratory, Oak Ridge, Tennessee 37831, USA*
[4]*Instituto de Física Rosario (CONICET) and Universidad Nacional de Rosario, Rosario, Argentina*
[5]*Neutron Scattering Division and Shull-Wollan Center, Oak Ridge National Laboratory; Oak Ridge, Tennessee 37831, USA*

*Corresponding author: parkp@ornl.gov, stonemb@ornl.gov, halaszg@ornl.gov, and christiansad@ornl.gov

Supplementary Notes

Crystal field levels of Single-ion Co^{2+} with spin-orbit coupling and trigonal distortion of ligand octahedron. The significant XXZ anisotropy of $Ba_2La_2CoTe_2O_{12}$ (BLCTO) presented in this work can be understood by a combination of spin-orbital entangled Kramers doublet and trigonal distortion. This can be described by the following single-ion Hamiltonian[1]:

$$H = \lambda_{\mathrm{SOC}}(\mathbf{L}\cdot\mathbf{S}) + \delta\left(L_z^2 - \frac{2}{3}\right), \quad (1)$$

where λ_{SOC} is a spin-orbit coupling constant for single-ion Co^{2+}, δ is a trigonal crystal field energy, and **L** (**S**) is an orbital (spin) angular momentum operator. A typical value of λ_{SOC} for Co^{2+} is known to be approximately 26 meV, with possible material-dependent deviations of around 2 meV, depending on additional covalency effects[1,2]. Also, positive δ corresponds to trigonal compression, which is the case of BLCTO. We can obtain an energy level diagram shown in Fig. 2e (the Kramer's doublet ground state was set to 0 meV) by diagonalizing Eq. 1. While the excitation energy from the J_{eff} = 1/2 to J_{eff} = 3/2 state is $\frac{3}{2}\lambda_{\mathrm{SOC}}$ ~ 39 meV when $\delta = 0$, finite δ gradually decreases this excitation energy.

In BLCTO, the above excitation energy was measured as 25.57 meV at 300 K; see the inelastic neutron scattering (INS) spectra in Supplementary Fig. 3a. Indeed, this is much smaller than the excitation energy expected for $\delta = 0$, indicating sizable δ. Note that the increase of the excitation energy at lower temperatures is attributed to magnetic correlation effects. Thus, the underlying situation of Eq. 1, which does not include magnetism, is better represented by the measurement at high temperature. A quantitative fitting to the 25.57 meV yields $\delta/\lambda_{\mathrm{SOC}}$ = 1.854 (see Fig. 2e). Such a large trigonal crystal field is consistent with the crystal structure of BLCTO with significant trigonal compression (see Supplementary Table 1).

Estimating the anisotropic *g*-factor. In a Co^{2+} spin system with the J_{eff} = 1/2 ground state, large trigonal compression leads to strong anisotropy of its *g*-factor[1-3], in addition to the XXZ anisotropy. As a result, the ratio g_{ab}/g_c (g_{ab} (g_c) is the *g*-factor for an in-plane (out-of-plane) magnetic field) of BLCTO is expected to deviate from 1. Meanwhile, different g_{ab}/g_c values can lead to distinct magnetic excitation spectra since g_{ab}^2 and g_c^2 is multiplied to in-plane (S_{xx} or S_{yy}) and out-of-plane (S_{zz}) dynamical spin correlations in the INS intensity formula, respectively. Therefore, identifying a precise value of g_{ab}/g_c is important to provide a correct comparison between INS data and spin dynamics simulations.

We estimated the g_{ab}/g_c of BLCTO using two different methods, the results of which are consistent with each other. First, g_{ab}/g_c can be calculated from the ground state wave functions of Eq. 1. The details of this calculation can be found in Ref. [1]. Supplementary Fig. 3b shows the calculated g_{ab} and g_c as a function of $\delta/\lambda_{\mathrm{SOC}}$. Using $\delta/\lambda_{\mathrm{SOC}}$ = 1.854 obtained from our INS data, we have g_{ab}/g_c = 1.77. Another method is utilizing the experimental *M–H* curve of powder BLCTO in Ref. [4]. The *M-H* curve shows two different saturation fields: $H_{s1} = H_{s,ab}$ = 32 T and $H_{s2} = H_{s,c}$ = 41 T. This is attributed to the XXZ anisotropy of exchange interactions (Δ, see Eq. 1 in the main text) and anisotropic *g*-factor (g_{ab}/g_c). The relation between these three quantities can be written as the following[4,5]:

$$\frac{H_{s,c}}{H_{s,ab}} = \frac{1+2\Delta}{3}\frac{g_{ab}}{g_c}. \quad (2)$$

Using $H_{s,c}/H_{s,ab}$ = 1.281 and Δ = 0.56 obtained from the fitting of paramagnetic scattering profiles without J_2 (Fig. 3), we obtain g_{ab}/g_c = 1.81 from Eq. 2. This is very close to g_{ab}/g_c = 1.77 estimated from the first method. All spin dynamics simulations included in this work used g_{ab}/g_c = 1.81. In addition, the absolute values of g_{ab} and g_c can be estimated using $g_{avg} = (2g_{ab} + g_c)/3 = 4.2$, which is derived from the saturation magnetization of powder BLCTO [4]. As a result, we obtained g_{ab} = 4.938 and g_c = 2.724.

Estimation of second nearest-neighbor exchange interactions (J_2). Here, we argue the plausible range of J_2 in BLCTO, which is an important variable to the phase diagram presented in Fig. 1. Given that the theoretical calculations do not match perfectly with the data for $T < T_N$, estimating J_2 from the low temperature spectra is subject to ambiguity. Instead, we analyzed J_2 using the results for $T > T_N$, following the same approach as introduced in Fig. 3. Supplementary Fig. 6 shows an overall effect of finite J_2 on the paramagnetic excitation spectrum: it generally broadens a spectrum along the |**Q**|-axis (see also Supplementary Fig. 8a). Yet, owing to its smaller magnitude, this effect is less significant compared to that of Δ, resulting in substantial degree of uncertainty of J_2 from our analysis (~ 30 %). Nevertheless, the goodness-of-fit to our paramagnetic excitation spectra identifies a well-defined global minimum of $\chi^2(J_1, J_2, \Delta)$ at J_1 = 2.7 meV, $J_2 = 0.03(1)J_1$, and Δ = 0.54(3) across a vast three-dimensional parameter space: 2 meV < J_1 < 2.9 meV, 0 < J_2/J_1 < 0.15, and 0.3 < Δ < 1.0 (see Supplementary Figs. 6 and 8b–e). This result again demonstrates Δ much smaller than 1 (*i.e.* significant XXZ anisotropy), in accordance with the optimal parameters derived in the absence of J_2 (J_1 = 2.62 meV, Δ = 0.56(2)).

Bond-dependent anisotropic exchange interaction terms in BLCTO. Here, we discuss the bond-dependent anisotropic exchange interactions in BLCTO 1) from a crystal structure perspective and 2) based on our analysis of paramagnetic excitation spectra with the generalized spin Hamiltonian. Extended from the J_1–J_2–Δ model argued above, the generalized spin Hamiltonian can be written in the crystallographic axes frame (x // the a-axis) as [6,7]:

$$\begin{aligned} H = \sum_{<i,j>_1} & J_1\left(S_i^x S_j^x + S_i^y S_j^y + \Delta S_i^z S_j^z\right) + 2J_{\pm\pm}\left[\left(S_i^x S_j^x - S_i^y S_j^y\right)\cos\phi_\alpha - \left(S_i^x S_j^y + S_i^y S_j^x\right)\sin\phi_\alpha\right] \\ & + J_{z\pm}\left[\left(S_i^y S_j^z + S_i^z S_j^y\right)\cos\phi_\alpha - \left(S_i^x S_j^z + S_i^z S_j^x\right)\sin\phi_\alpha\right] \\ & + \sum_{<i,j>_2} J_2\left(S_i^x S_j^x + S_i^y S_j^y + \Delta S_i^z S_j^z\right), \end{aligned} \quad (3)$$

where $\langle i,j\rangle_n$ runs over the bonds between n^{th} nearest neighbours, and $\phi_\alpha = \{0, \frac{2\pi}{3}, -\frac{2\pi}{3}\}$ is a bond-dependent angle that follows the C_3 rotation symmetry with the c-axis.

From a crystal structure perspective, it is important to point out that the edge-shared octahedron network between J_{eff} = 1/2 magnetic ions are required for the microscopic mechanism of bond-dependent anisotropic interactions suggested by Jackeli and Khaliullin[1,2,8,9]. On the other hand, the CoO_6 octahedra in BLCTO are fully isolated from each other (see Fig 2a). Consequently, $J_{\pm\pm}$ and $J_{z\pm}$ would be less significant in BLCTO compared to the previous Co Kitaev systems with the edge-shared configuration (e.g. see Ref. [10]). The case of $Ba_3CoSb_2O_9$ is a nice example of such: the CoO_6 octehedra are also isolated in this material, and its spin-wave spectrum has thus far been discussed without accounting for bond-dependent off-diagonal interaction terms[11,12].

Nevertheless, the above argument does not guarantee $J_{\pm\pm}$ and $J_{z\pm}$ is negligible (see the main text). Thus, we further estimated $J_{\pm\pm}$ and $J_{z\pm}$ in BLCTO by comparing the paramagnetic excitation spectra in Fig. 3a and LLD simulations of the J_1–J_2–Δ–$J_{\pm\pm}$–$J_{z\pm}$ model. However, with more than three parameters (J_1, J_2, Δ, $J_{\pm\pm}$, $J_{z\pm}$), a brute-force scan of goodnees-of-fit (χ^2) throughout the entire parameter space (such as Supplementary Fig. 8b) is not achievable due to an extremely long computation time (> 1 month). Therefore, we adopted the Bayesian optimization algorithm to search for a parameter set (J_1, J_2, Δ, $J_{\pm\pm}$, $J_{z\pm}$) that minimizes the chi-square between the measured and calculated dynamical structure factors $S(|\mathbf{q}|, \omega)$. The choice of this particular algorithm is because an LLD simulation is time consuming – it takes 2~3 minutes to generate each spectrum in Fig. 3b–c. Thus, it is very important to minimize the number of times LLD simulations are performed. In this respect, Bayesian optimization is an ideal methodology as it is gradient-free and reaches an optimal solution very fast through a smart suggestion of the optimal parameter set based on surrogate model and acquisition function[13]. We used the Bayesian optimization package implemented in *Python*, which uses Gaussian process for the surrogate model[14,15].

Supplementary Fig. 15 shows the sampled parameter sets over the 200 iterations of Bayesian optimization, where the y-axis is the chi-sqaure (χ^2) described in the Methods section. No noticeable improvement of χ^2 was found compared to the minimum χ^2 found in the J_1–J_2–Δ model (red circles in Supplementary Fig. 15). Given the distribution of χ^2 as a function of each parameter, the optimal values and uncertainties of the exchange parameters are: $J_1 \sim 2.69(7)$ meV, $J_2 \sim 0.02(2)J_1$, $\Delta \sim 0.49(4)$, $J_{\pm\pm} \sim 0.00(2)\ J_1$, and $J_{z\pm} \sim 0.0(15)\ J_1$. Notably, the J_1, J_2, and Δ values obtained from the optimization are almost the same as those determined from the J_1–J_2–Δ model (J_1 = 2.7 meV, $J_2 = 0.03(1)J_1$, and Δ = 0.54(3)). Another remark is that χ^2 is very sensitive to $J_{\pm\pm}$, while it gives a large uncertainty of $J_{z\pm}$ roughly ranging from $-0.15J_1$ to $0.15J_1$. To address $J_{z\pm}$ more accurately, obtaining four-dimensional $S(\mathbf{Q}, \omega)$ from single-crystal BLCTO is essential. Nevertheless, considering the prior section discussing J_2, the current analysis demonstrates the validity of the minimal J_1–Δ model with strong planar-type XXZ anisotropy as the effective spin Hamiltonian of BLCTO.

The nearly-gapless excitation spectra of BLCTO is another crucial feature relevant to $J_{\pm\pm}$ and $J_{z\pm}$. The presence of bond-dependent off-diagonal interaction terms generally leads to a gapped mode, whereas our INS data encompassing the sub-meV region does not show a clear indication of an energy gap (see Supplementary Fig. 17). However, caution is needed when interpreting the vanishing energy gap as an indication of negligible $J_{\pm\pm}$ and $J_{z\pm}$. Despite finite $J_{\pm\pm}$ and $J_{z\pm}$, this energy gap does not appear in LSWT due to the accidental $U(1)$ degeneracy[7], implying the requirement of quantum

fluctuations (*e.g.* higher-order corrections in LSWT) to account for the gap. Even with quantum fluctuations, the energy gap induced by such a mechanism are generally very small. Consequently, a spin system may still exhibit a nearly-gapless excitation mode at the magnetic zone center even with sizable bond-dependent off-diagonal terms and quantum fluctuations.

Schwinger Boson Theory. The Hamiltonian of the XXZ-model with nearest-neighbor exchange interactions is

$$\hat{\mathcal{H}} = \sum_{\langle ij \rangle} J_{ij} (\hat{S}_i^x \hat{S}_j^x + \hat{S}_i^y \hat{S}_j^y + \Delta \hat{S}_i^z \hat{S}_j^z) \tag{4}$$

with $0 < \Delta < 1$ for easy-plane anisotropy. The spin-1/2 operators are expressed in terms of Schwinger bosons,

$$\hat{\boldsymbol{S}}_i = \frac{1}{2} \hat{\boldsymbol{b}}_i^\dagger \boldsymbol{\sigma} \hat{\boldsymbol{b}}_i \tag{5}$$

where $\hat{\boldsymbol{b}}^\dagger = (\hat{b}_{i\uparrow},\ \hat{b}_{i\downarrow})$ and $\boldsymbol{\sigma} \equiv (\sigma^x, \sigma^y, \sigma^z)$ are the vector of Pauli matrices, that satisfy the local constraint $\hat{b}_{i\uparrow}^\dagger \hat{b}_{i\uparrow} + \hat{b}_{i\downarrow}^\dagger \hat{b}_{i\downarrow} = 1$. In the Schwinger boson theory (SBT), the spin-spin interaction can be expressed in terms of bond operators as[11,16–17]:

$$\begin{aligned} J_{ij}(\hat{S}_i^x \hat{S}_j^x + \hat{S}_i^y \hat{S}_j^y + \Delta \hat{S}_i^z \hat{S}_j^z) = &- J_{ij}^+ (1+\varepsilon_1)\ \hat{A}_{ij}^\dagger \hat{A}_{ij}\ + J_{ij}^+ (1-\varepsilon_1) : \hat{B}_{ij}^\dagger \hat{B}_{ij} : \\ &- J_{ij}^- (1+\varepsilon_2) : \hat{C}_{ij}^\dagger \hat{C}_{ij} : + J_{ij}^- (1-\varepsilon_2) \hat{D}_{ij}^\dagger \hat{D}_{ij} + (J_{ij}^+ \varepsilon_1 + J_{ij}^- \varepsilon_2) S^2 \end{aligned} \tag{6}$$

with $J_{ij}^+ = J_{ij}(1+\Delta)/2$, $J_{ij}^- = J_{ij}(1-\Delta)/2$ and,

$$\hat{A}_{ij}^\dagger = \frac{1}{2} \sum_{\sigma=\uparrow\downarrow} \sigma \hat{b}_{i\sigma}^\dagger \hat{b}_{j\bar{\sigma}}^\dagger \qquad \hat{B}_{ij}^\dagger = \frac{1}{2} \sum_{\sigma=\uparrow\downarrow} \hat{b}_{i\sigma}^\dagger \hat{b}_{j\sigma} \tag{7}$$

$$\hat{C}_{ij}^\dagger = \frac{1}{2} \sum_{\sigma=\uparrow\downarrow} \sigma \hat{b}_{i\sigma}^\dagger \hat{b}_{j\sigma} \qquad \hat{D}_{ij}^\dagger = \frac{1}{2} \sum_{\sigma=\uparrow\downarrow} \hat{b}_{i\sigma}^\dagger \hat{b}_{j\bar{\sigma}}^\dagger. \tag{8}$$

The bond operator description introduces continuous parameters, ε_1 and ε_2, that represent different saddle-point (SP) approximations[18]. These parameters control the relative weights of the anomalous (pairing) ($\hat{A}_{ij}^\dagger$ and $\hat{D}_{ij}^\dagger$) and normal (hopping) ($\hat{B}_{ij}^\dagger$ and $\hat{C}_{ij}^\dagger$) operators[19]. Both parameters were determined by fitting the magnon dispersion obtained with the Series Expansion (SE) method [20–22].

To compute the dynamical spin structure factor (DSSF), we use a large-N theory (N is the number of flavors in the boson fields) based on the Feynman path integral formulation[23–24]. In this formulation, the partition function is written as:

$$\mathcal{Z}[h] = \int [D\bar{b}b][D\lambda] e^{-\int_0^\beta d\tau [\sum_{i\sigma} \bar{b}_{i\sigma} \partial_\tau b_{i\sigma} + \mathcal{H}(\bar{b},b) + i \sum_i \lambda_i (\sum_\sigma \bar{b}_{i\sigma} b_{i\sigma} - 2S) + \sum_{\mu\alpha\beta i} h_i^\mu(\tau) \frac{1}{2} \bar{b}_{i\alpha} \sigma_{\alpha\beta}^\mu b_{i\beta}]} \tag{9}$$

where the complex fields $\bar{b}$ and b are the eigenvalues of the Schwinger boson operators acting on coherent states, $\beta = 1/k_B T$, λ is the Lagrange multiplier introduced to impose the constraint of one boson per site, and $\boldsymbol{h}$ is the external magnetic field. Due to the quartic nature of the Hamiltonian in the boson fields, we employ the Hubbard-Stratonovich (HS) transformation to decouple them,

$$e^{J_{ij}\bar{X}_{ij}X_{ij}} = \int \frac{d\bar{W}^X_{ij}dW^X_{ij}}{2\pi i}\; e^{(-\bar{W}^X_{ij}W^X_{ij}+\sqrt{|J_{ij}|}\bar{X}_{ij}W^X_{ij}+\mathrm{sgn}(J_{ij})\sqrt{|J_{ij}|}\bar{W}^X_{ij}X_{ij})} \tag{10}$$

where a HS field W^X is introduced for each bond field $X = A, B, C, D$. The phases of these HS fields and the Lagrangian multiplier are the gauge fields of the theory. By integrating out the resulting quadratic action in the bosonic fields, we obtain the exact partition function

$$\mathcal{Z}[h] = \int [D\bar{\phi}D\phi]\; e^{-S_{\text{eff}}(\bar{\phi},\phi,h)} \tag{11}$$

where S_{eff} is the effective action which is a function of the auxiliary fields $\bar{\phi}_\alpha = (W^X_{ij}, \bar{W}^X_{ij}, \lambda)$.

The lowest-order contribution of the large-N expansion corresponds to the SP approximation

$$\left.\frac{\partial S_{\text{eff}}(\bar{\phi},\phi,h=0)}{\partial \phi_\alpha}\right|_{\text{sp}} = \left.\frac{\partial S_{\text{eff}}(\bar{\phi},\phi,h=0)}{\partial \bar{\phi}_\alpha}\right|_{\text{sp}} = 0. \tag{12}$$

For the spin Hamiltonian of the triangular lattice antiferromagnet under consideration, the magnetic order emerges at the SP level as a Bose-Einstein condensation of the Schwinger Bosons. As emphasized in the study by Zhang et al. [17], selecting a non-fragmented boson condensate is essential to yield a finite correction from the specific $1/N$ contribution introduced below.

The Dynamical Spin Susceptibility is computed from the partition function as

$$\chi_{\alpha\beta}(\boldsymbol{q},\omega) = \frac{\partial^2 \ln \mathcal{Z}[h]}{\partial h^\alpha_{\boldsymbol{q},\omega}\, \partial h^\beta_{-\boldsymbol{q},-\omega}} \tag{13}$$

where $h^\alpha_{\boldsymbol{q},\omega}$ is the α component of the external magnetic field in momentum and frequency space. Expanding the effective action as outlined in the previous work[25], we obtain the dynamical susceptibility beyond the SP approximation by incorporating the Gaussian fluctuations of the auxiliary fields,

$$\chi_{\alpha\beta}(\boldsymbol{q},\omega) = \chi^{sp}_{\alpha\beta}(\boldsymbol{q},\omega) + \chi^{fl}_{\alpha\beta}(\boldsymbol{q},\omega) \tag{14}$$

where $\chi^{sp}_{\alpha\beta}$ is the SP contribution, and $\chi^{fl}_{\alpha\beta}$ is a $1/N$ correction that includes a singular contribution of order one which cancels the residues of the single-spinon poles of $\chi^{sp}_{\alpha\beta}$ (i.e. it acts as a counter-diagram for the SP diagram)[17]. These two contributions are diagrammatically represented as in Supplementary Fig. 18, where the free-spinon propagator $\mathcal{G}^{\text{sp}}$ is represented by the solid lines, the external vertices are given by $u^\alpha(\boldsymbol{q},\omega) \equiv \partial\mathcal{G}^{-1}/\partial h^\alpha_{\boldsymbol{q},\omega}$ couple the spinons to the external fields ϕ, the internal vertices as $v_\phi \equiv \partial\mathcal{G}^{-1}/\partial\phi$ couple the spinons to the auxiliary fields, the propagator of the auxiliary fields, also known as random phase approximation (RPA) propagator, is given by the inverse of fluctuation matrix $S^{(2)}_{\alpha\beta} \equiv \frac{1}{2}(\partial^2 S_{\text{eff}}/\partial\phi_\alpha\partial\phi_\beta)|_{\text{sp}}$.

Finally, the fluctuation-dissipation theorem states that

$$S^{\alpha\beta}(\boldsymbol{q},\omega) = \frac{1}{\pi}\mathrm{Im}[\chi_{\alpha\beta}(\boldsymbol{q},\omega)] \tag{15}$$

at zero temperature, where $S^{\alpha\beta}$ is the dynamical spin structure factor (DSSF) measured with inelastic neutron scattering.

As we already mentioned, the parameters ε_1 and ε_2 in Eq. (6) represent a family of SP solutions. To determine the *optimal* decoupling scheme, we compared the magnon dispersion of the SBT with SE results across a range of anisotropy values, from the isotropic limit ($\Delta = 1$)

to the XY-limit ($\Delta = 0$). As detailed in Ref. [17], the introduction of Gaussian corrections to the DSSF mitigates the sensitivity to variations in the decoupling scheme. Additionally, in the large-S limit, the LSWT result is consistently obtained, irrespective of the chosen decoupling scheme.

Supplementary Fig. 19 shows the comparison of the magnon dispersion obtained with SE and the DSSF for the *optimal* decoupling scheme for thse cases $\Delta = 1.0$, 0.8 and 0.6. For simplicity, the cases with $\Delta = 0.4, 0.0$ and the isotropic case with $J_2 = 0.02J_1, 0.04J1$ are not shown. Empirically, we have observed that the optimal decoupling scheme adheres to the following relationship: $\varepsilon_1 = -0.1 + 0.4/(1+\Delta)$ and $\varepsilon_2 = -0.35$. We highlight that this empirical law matches the decoupling scheme used for the nearly isotropic triangular antiferromagnets $Ba_3CoSb_2O_9$ [11] and for $KYbSe_2$ [16]. The main effect of increasing the parameter ε_1 is to enlarge the bandwidth of the magnon dispersion and to lower the magnon peak at K and K' in relation with the bandwidth. Additionally, a negative ε_2 narrows the magnon bandwidth and transfers spectral weight from the magnon peaks to the continuum. By carefully adjusting the values of ε_1 and ε_2, we were able to accurately match the shape and energy scale of the SE magnon dispersion, with the exception of the roton-like minimum at M mode, as we pointed out in Ref. [11]. In the SE calculation, the roton-like minimum persists in the whole range of anisotropies from $\Delta = 1$ to 0.

In the XY-limit, the SBT successfully replicates the SE magnon dispersion, albeit with the majority of the spectral weight residing in the two-spinon continuum. However, given that the XY-model is farther from the quantum melting point that signals the continuous transition into a spin liquid phase, a semiclassical treatment, such as the non-linear spin wave approach might provide a more accurate description of the DSSF. As previously noted in Ref. [17], the SBT is most appropriate near the isotropic scenario, which is in closer proximity to the spin liquid phase[26,6].

Comparison between the spin model and the experimental *M–H* curve. The experimental *M–H* curve reported in Ref. [4], which show saturation field values and the trace of a 1/3-magnetization plateau phase, provide a good opportunity to crosscheck the exchange parameters of BLCTO derived in this study. The saturation fields perpendicular (H_s^{ab}) and parallel (H_s^c) to the *c*-axis are extracted to be 32 T and 41 T, respectively in Ref. [4]. However, there is some ambiguity in these values due to the smooth variation of the *M–H* curve around the saturation, likely due to powder averaging in conjunction with anisotropic *g*-factors, and strong planar XXZ anisotropy ($\Delta < 1$). A fairer estimation of H_s^{ab} and H_s^c considering these uncertainties and based on the *dM*/d*H* curve would be approximately 30±2 T and 40±2 T.

H_s^c and H_s^{ab} for the J_1–Δ model are estimated as follows using the linear spin-wave theory (see Ref. [5]):

$$H_s^{ab} = \frac{J_1 S\left(9 + 4(J_c / J_1)\right)}{g_{ab}\mu_B} \tag{16}$$

$$H_s^c = \frac{J_1 S\left(3 + 6\Delta + 2(1+\Delta)(J_c / J_1)\right)}{g_c \mu_B}, \tag{17}$$

where J_c is the interlayer coupling strength, g_{ab} (g_c) is the *g*-factor perpendicular to (along) the *c*-axis, and $\mu_B = 0.05788$ meV/T. Using the anisotropic *g*-factors presented in the previous Supplementary Note and the optimal parameter set [J_1 = 1.77 meV, Δ = 0.56, J_2 = 0] with J_c = 0 (J_1 = 1.77 meV is from the Schwinger Boson calculation result in Fig. 4), we obtain H_s^{ab} = 27.9 T and H_s^c = 35.7 T, respectively. A more realistic assumption, $J_c \sim 0.05J_1$, yields H_s^{ab} = 28.5 T and H_s^c = 36.6 T. These values are 90~95 % of the experimental saturation fields.

Several factors may contribute to the 5~10% underestimation of H_s^{ab} and H_s^c. First, introducing $J_2 = 0.03J_1$ to the model (see Supplementary Fig. 8) increases optimal J_1 derived from the Schwinger Boson theory to 1.87 meV, 6 % larger than J_1 = 1.77 meV (Supplementary Fig. 13). While this will likely reduce the underestimation of the saturation fields, further quantitative estimation is limited by unclear effects of J_2 on the *M–H* curve. Another factor could be the influence of $J_{z\pm}$ on the saturation field, which may range from $-0.15J_1$ to $0.15J_1$ according to our LLD analysis (see Supplementary Notes above). Indeed, this effect was not included in either the Schwinger Boson calculation or the theoretical estimation of the *M–H* curve. Thus, given the simplicity of the J_1–Δ model suffering from the systematic errors, achieving 90~95 % consistency in the saturation field analysis is reasonable.

The position of the 1/3-magnetization plateau in the *M–H* curve can provide additional diagnostic insights into our parameter set, although it is subject to greater systematic errors compared to the saturation field analysis. A rough crosscheck of J_1 can be made by comparing the experimental ($9 < H < 16$ T) and simplified theoretical ($H_{1/3} \sim 3J_1S / g_{ab}\mu_B$, see Ref. [5]) field position of this plateau phase. A combination of J_1 = 1.77 and the *g* factors presented in Supplementary Notes results in $H_{1/3}$ = 9.3 T, aligning with the experimental plateau range. Nevertheless, we caution more quantitative interpretations. First, the smoothly varying *M–H* curve gives rise to ambiguity in determining the precise range of the plateau phase (it is not perfectly flat). Second, the *M–H* curve in Ref. [4] was measured at finite temperature ($0.4T_N$), which could affect the plateau position and result in discrepancies with the theoretical estimation at T = 0 K [27]. Third, some systematic errors are expected due to the simplicity of the J_1–Δ model, as discussed above.

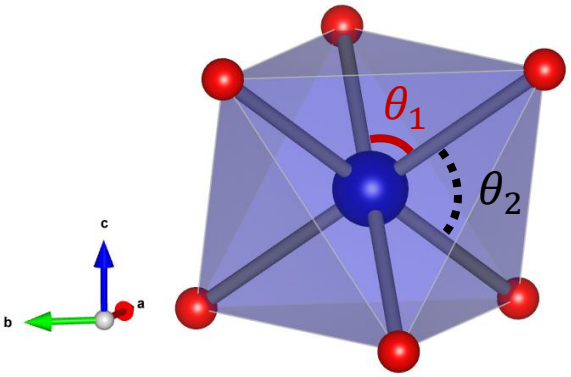

Supplementary Fig. 1 | CoX_6 octahedron (X = O, S) with its (111) parallel to the c-axis. The difference between θ_1 and θ_2, which is zero in a regular octahedron without distortion, quantifies the degree of trigonal distortion of a material. See Supplementary Table 1.

Supplementary Table 1 | Comparing the degree of trigonal distortion (θ_1 - θ_2) and XXZ anisotropy (Δ) in several Co^{2+} materials. The values are from Refs.[11,28-35]

	$\theta_1 - \theta_2$	Δ
$CoPS_3$	-9.28°	0.6
$Na_2BaCo(Po_4)_2$	6.56°	1.7
$Ba_3CoSb_2O_9$	-0.14°	0.935
$Ba_3CoNb_2O_9$	-0.34°	0.996
Ba_2CoTeO_6	0.1°	0.96
$Ba_2La_2CoTe_2O_{12}$ (This work)	**14.36°**	**0.54(3)**

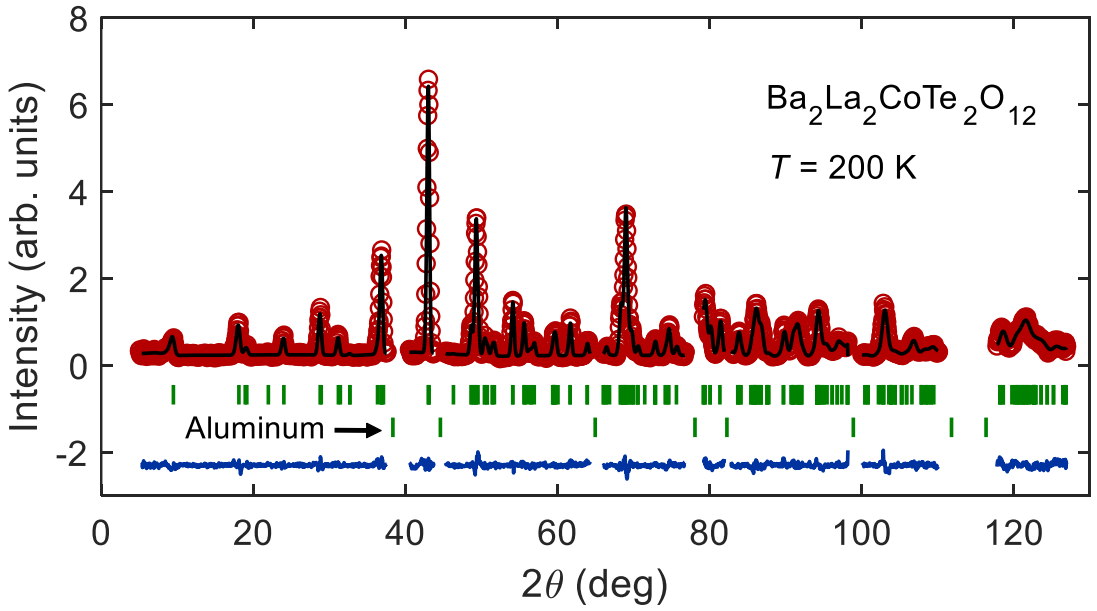

Supplementary Fig. 2 | Powder neutron diffraction profile of BLCTO. The data were collected at 200 K, using a constant neutron wavelength λ = 1.539 Å**.** A solid black line is the simulated pattern from the Rietveld refinement result which is consistent with the crystal structure reported in Ref. [4]. A solid blue line denotes the difference between the measured and simulated profile. 2θ regions close to the Bragg peaks of Aluminum sample holder (the second array of green vertical ticks) are masked and were excluded from the Rietveld refinement analysis.

Supplementary Table 2 | Crystal structure of BLCTO derived from the Rietveld refinement of the diffraction profile in Supplementary Fig. 2. The result is consistent with that reported in Ref. [4]

T = 200 K	Space group: *R* -3 (No. 148) Cell dimensions: *a*=*b*=5.7109(1) Å, *c*=27.6501(9) Å, α=β=90°, γ=120°			
Atom	Wychoff letter	x/*a*	y/*b*	z/*c*
Ba	6c	0	0	0.1365(2)
La	6c	0	0	0.2892(1)
Co	3a	0	0	0
Te	6c	0	0	0.4161(2)
O1	18f	0.4655(6)	0.4673(6)	0.1165(1)
O2	18f	0.4293(6)	0.4560(7)	0.2956(1)
	Overall *B* factor: 0.32(3) Å^2			
	Agreement factors: R_p (%) = 7.39, R_{wp} (%) = 9.41, R_{exp} (%) = 6.98, χ^2 = 1.82			

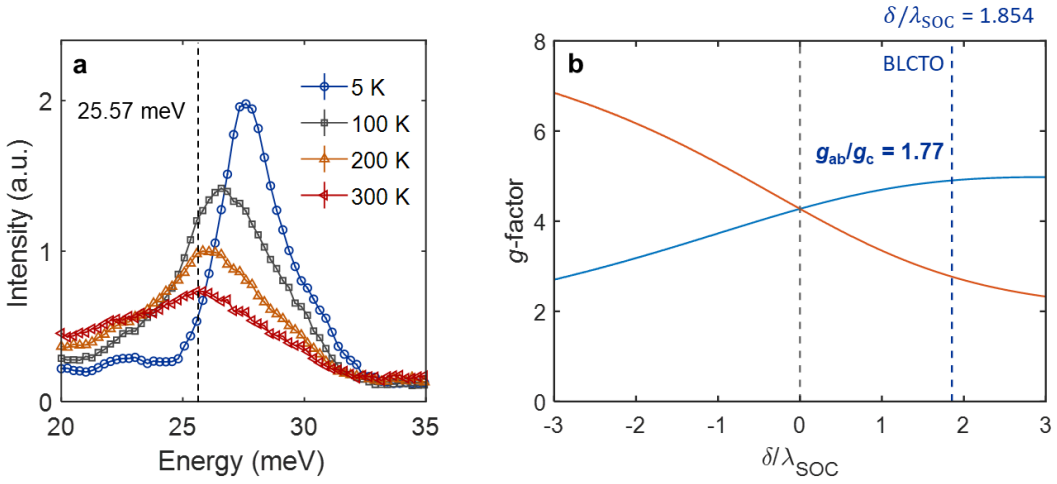

Supplementary Fig. 3 | Nature of the J_{eff} = 1/2 ground state in BLCTO. a, The J_{eff} = 1/2 → J_{eff} = 3/2 transitions of BLCTO at four different temperatures measured by INS. Error bars (= standard deviations) are much smaller than the data symbols. **b,** In-plane (g_{ab}) and out-of-plane (g_c) *g*-factors of the Co^{2+} Kramers' doublet ground state as a function of trigonal crystal field (δ), which are calculated from Eq. 1 in Supplementary Notes. A blue dashed line indicates the position of BLCTO (Δ/λ_{SOC} = 1.854)

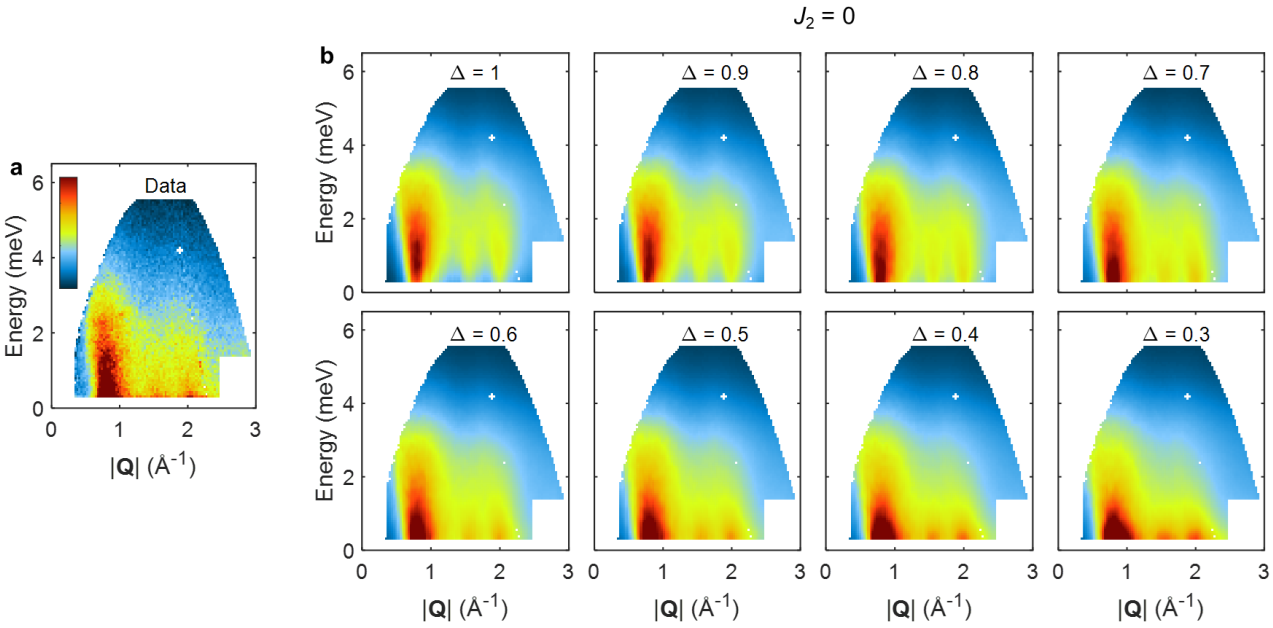

Supplementary Fig. 4 | Effects of XXZ anisotropy (Δ) on a powder-averaged paramagnetic excitation spectrum. a, The INS data from E_i = 6 meV and T = 5.3 K (1.63T_N) and **b**, corresponding simulations with different Δ and J_2 = 0 (see Methods).

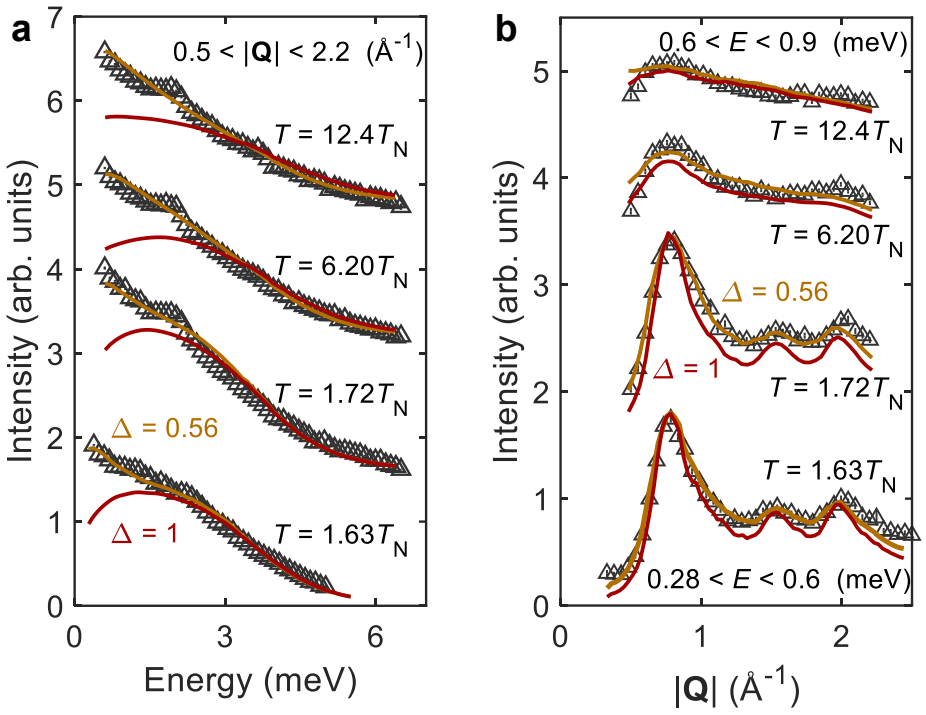

Supplementary Fig. 5 | Comparison between measured paramagnetic scattering profiles and LLD simulations with and without planar XXZ anisotropy. Orange (red) solid lines are the simulation results from Δ = 0.56 (1.0). The data and simulation plots of $T = 1.63T_N$ in **b** used the energy integration range from 0.28 to 0.6 meV. All other plots in **b** used the energy integration range from 0.6 to 0.9 meV. Error bars (= standard deviations) are much smaller than the data symbols.

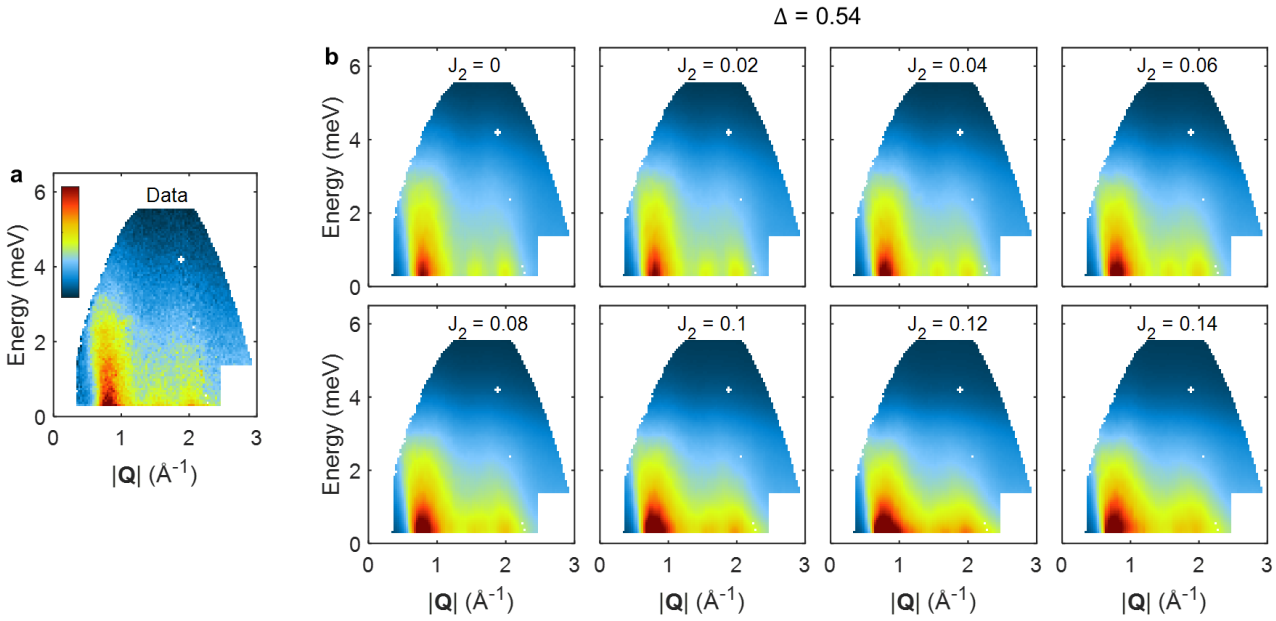

Supplementary Fig. 6 | Effects of J_2 on a powder-averaged paramagnetic excitation spectrum. **a**, The INS data from E_i = 6 meV and T = 5.3 K (1.63T_N) and **b** corresponding simulations with different J_2 and Δ = 0.54 (see Methods).

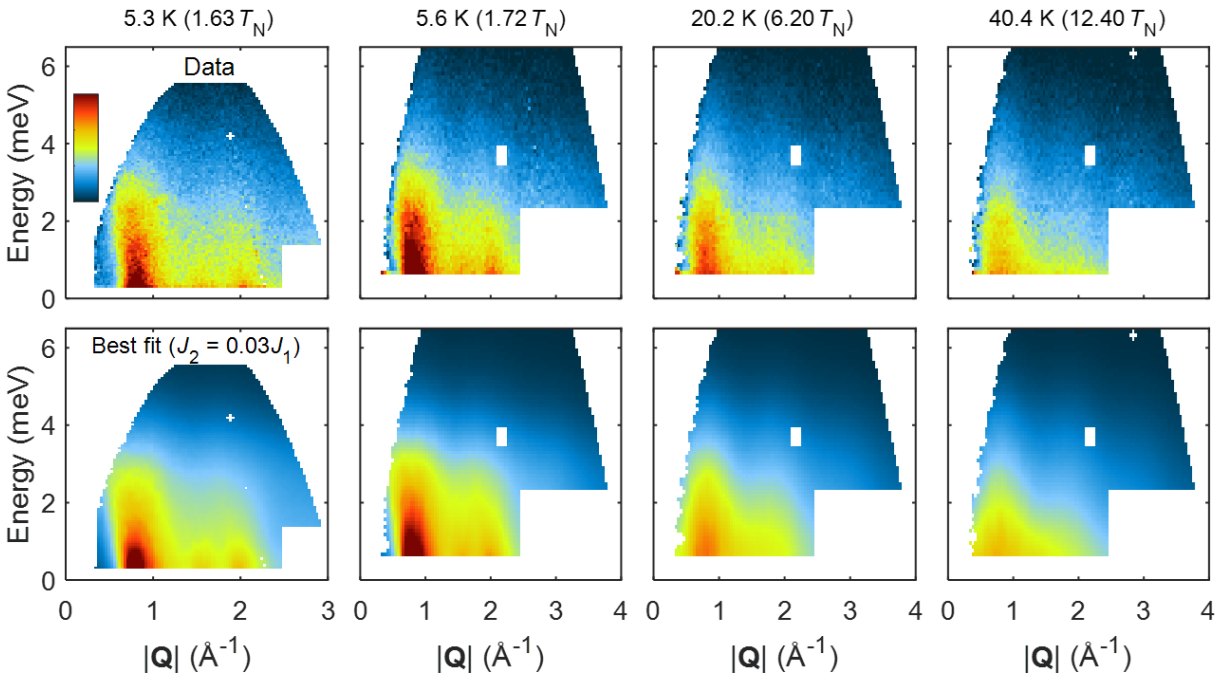

Supplementary Fig. 7 | Best fit of powder-averaged paramagnetic excitation spectra with finite J_2. a, The INS data of BLCTO same as those shown in Fig. 3a. **b**, The best fit of the LLD simulation to **a** with finite j_2: J_1 = 2.70(5) meV, J_2 = 0.03(1)J_1, and Δ = 0.54(2).

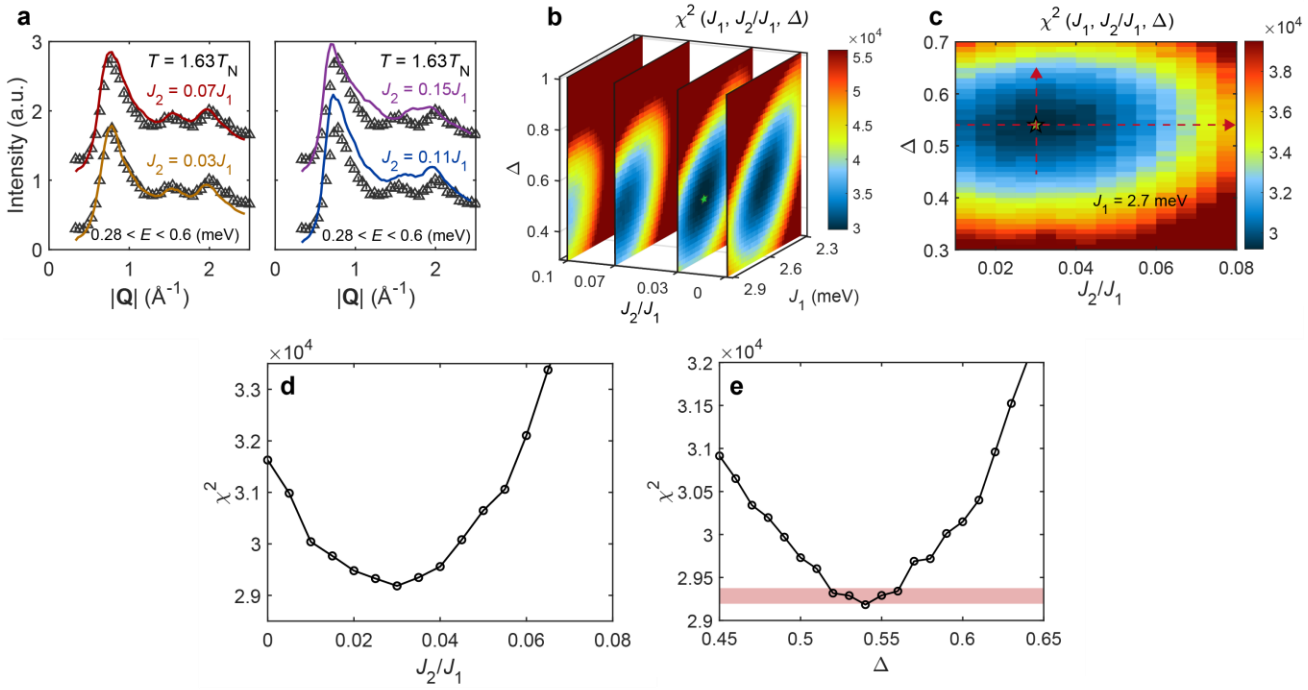

Supplementary Fig. 8 | Quantitative estimation of exchange parameters in the J_1–J_2–Δ model. **a**, Effect of J_2 on the low-energy excitation spectra of paramagnetic BLCTO. Error bars (= standard deviations) are much smaller than the triangular symbols. **b**–**c**, Calculated goodness-of-fit results to the data in Fig. 3a, across a wide three-dimensional parameter space of J_1, J_2, and Δ (see Methods). Green stars in **b**–**c** denote the positions of minimum χ^2, namely $J_1 = 2.70(5)$ meV, $J_2 = 0.03(1)J_1$, and $\Delta = 0.54(3)$. **d**–**e**, One-dimensional cuts of along the red dashed lines in **a**. The $\chi^2(J_1, J_2/J_1, \Delta)$ is not perfectly smooth due to a systematic uncertainties inherent in the analysis (e.g., the paramagnetic excitations are broad and the data is noisy). Therefore, the data points inside the red shaded regions in **b**–**c** are considered to have the equal goodness-of-fit, from which the uncertainty of our best fit was determined: $J_2 = 0.03 \pm 0.01$ and $\Delta = 0.54 \pm 0.02$. The uncertainty of the best fit without J_2 ($\Delta = 0.56 \pm 0.02$) was determined by the same method.

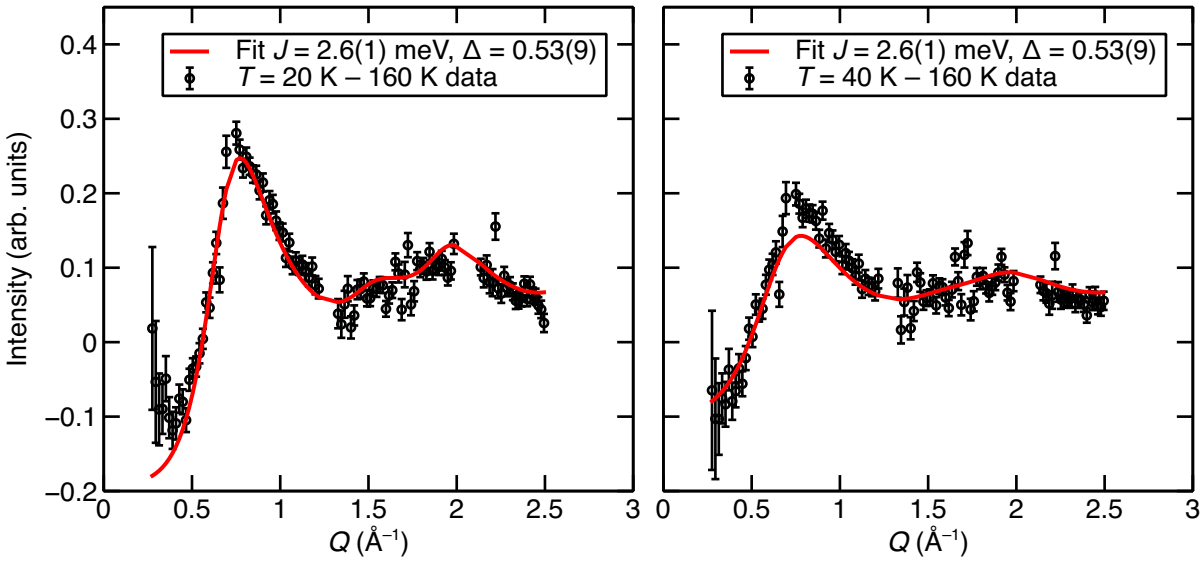

Supplementary Fig. 9 | Data with E_i = 10 meV (black circles) and model fits (red lines) to energy-integrated magnetic diffuse scattering data. 160 K data set was subtracted from the 20 and 40 K data to remove nuclear and background scattering. Data points near Bragg positions were excluded where this temperature subtraction introduced artifacts. Refinements of the values of J_1 and Δ were performed using the Spinteract software, details of which are provided in Ref. [36]. Spins were taken as classical vectors of length $[S(S+1)]^{1/2}$ (with S=1/2) and the g-factor ratio g_{ab}/g_c = 1.81 was included. An overall intensity scale factor was also optimized to match the experimental data. The results obtained from this approach, J_1 = 2.6(1) meV and Δ = 0.53(9), are in excellent agreement with those reported in the main text. Error bars indicate the standard deviation of each data point.

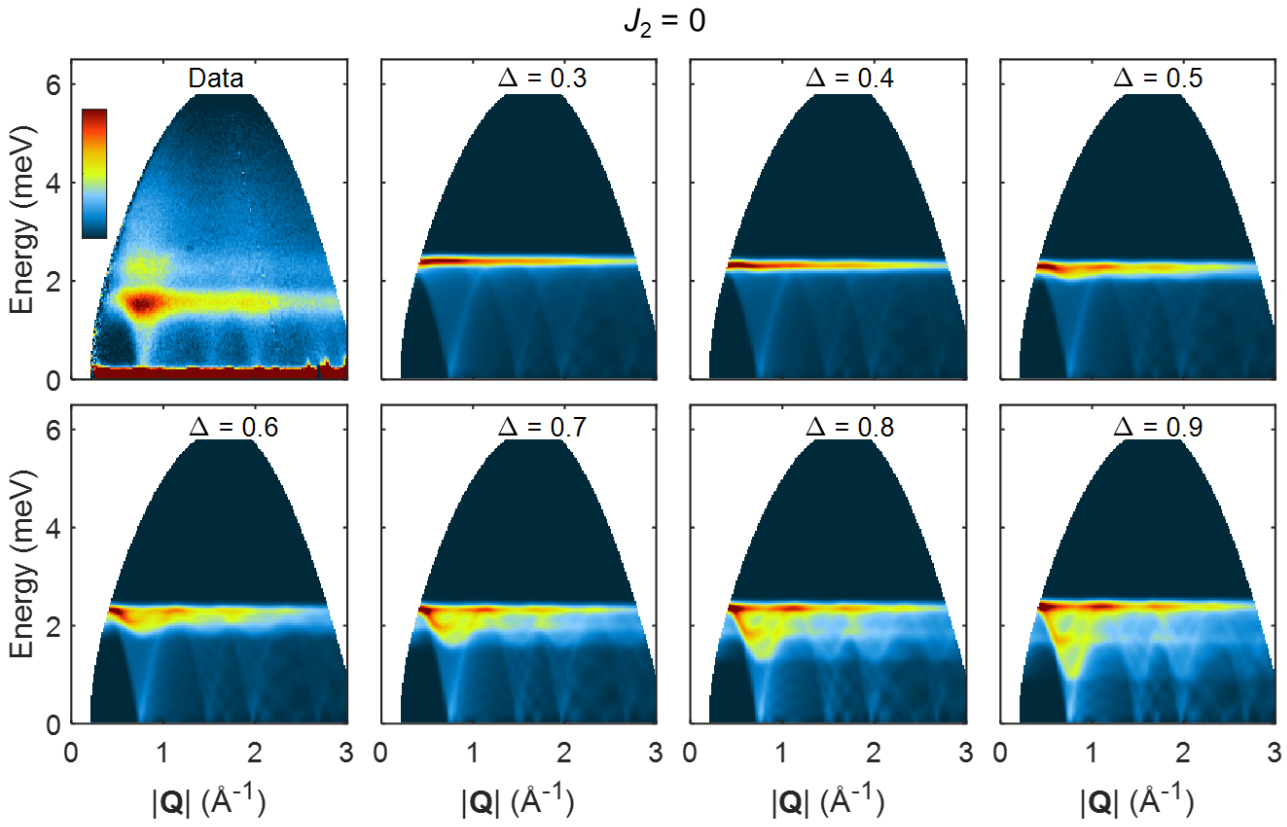

Supplementary Fig. 10 | Effects of XXZ anisotropy (*Δ*) on a powder-averaged spin-wave spectrum from linear spin-wave theory (LSWT). Top-left shows the INS data from E_i = 6 meV and T = 1.65 K (0.506 T_N) and the other panels show corresponding LSWT simulations with different *Δ* and J_2 = 0. We used J_1 = 1.55 meV.

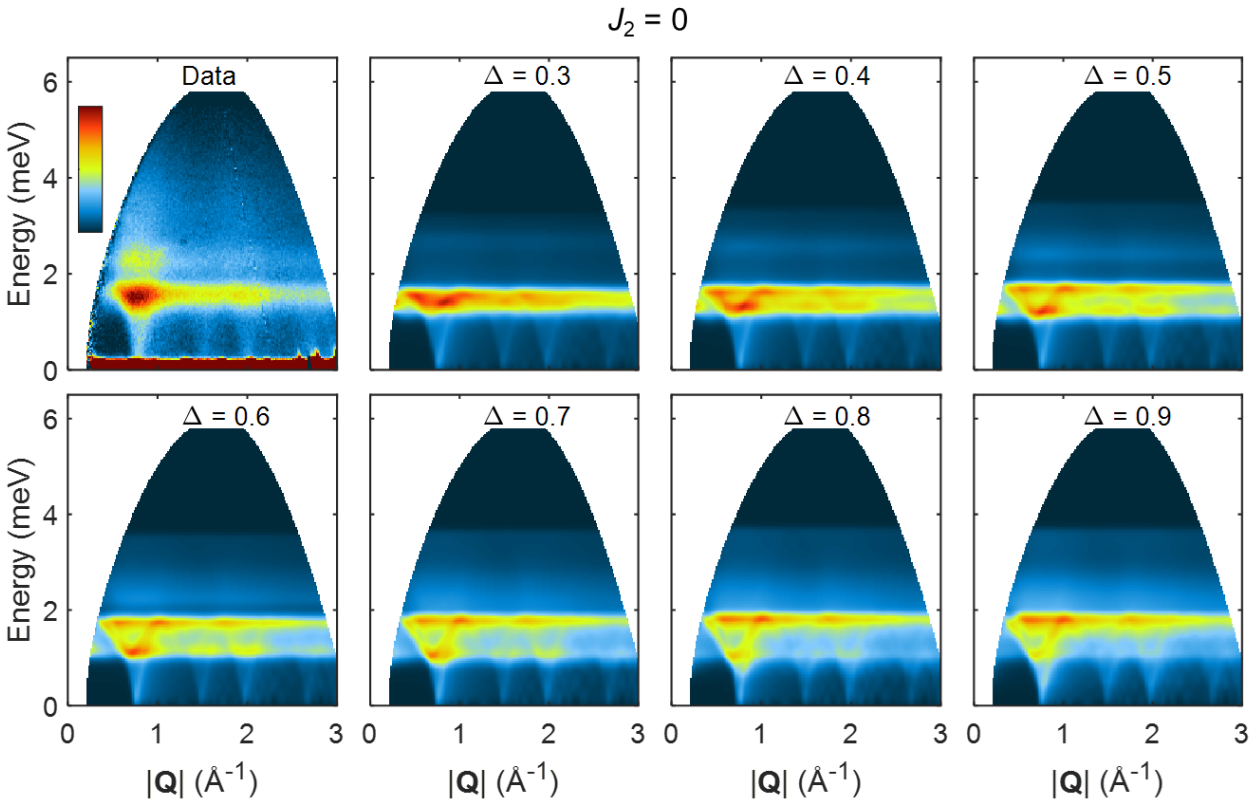

Supplementary Fig. 11 | Effects of XXZ anisotropy (Δ) on a powder-averaged spin-wave spectrum from non-linear spin-wave theory (NLSWT). Top-left shows the INS data from E_i = 6 meV and T = 1.65 K (0.506 T_N) and the other figures show corresponding NLSWT simulations with different Δ and J_2 = 0. We used J_1 = 1.55 meV.

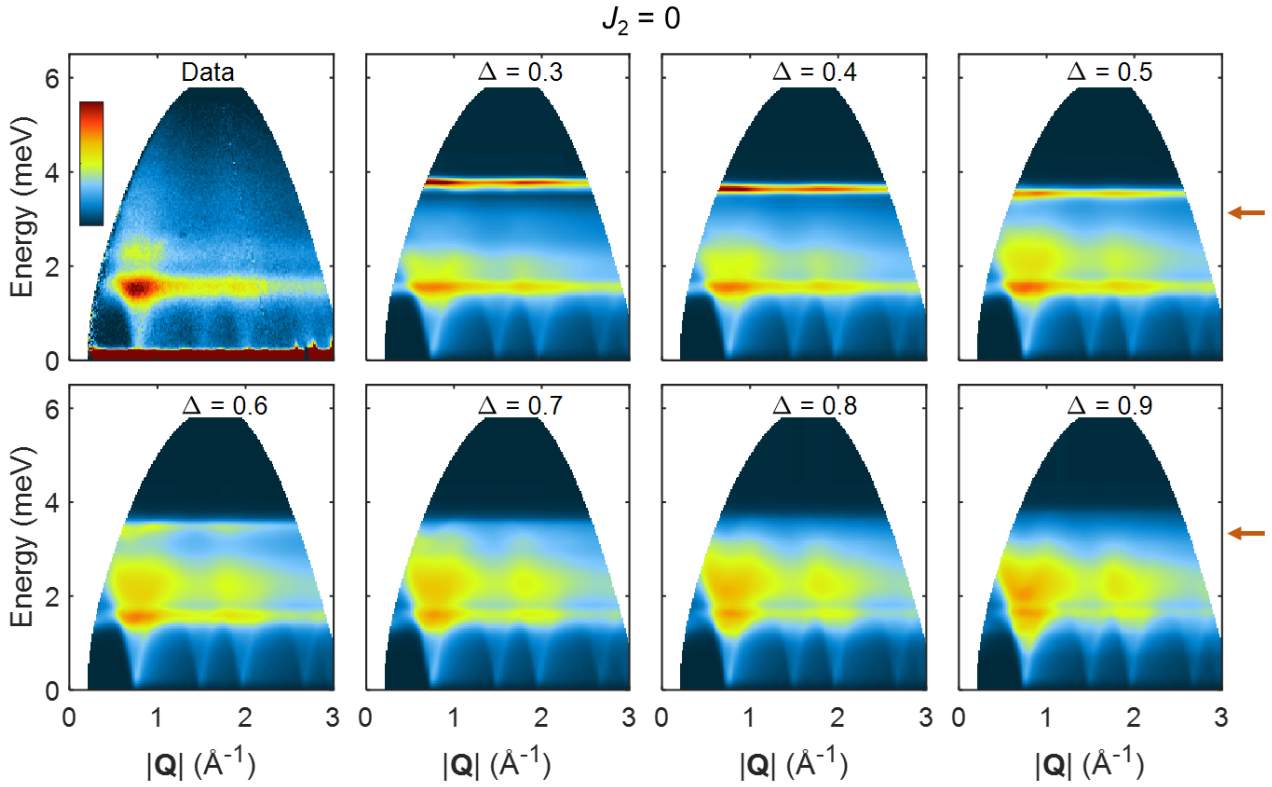

Supplementary Fig. 12 | Efects of XXZ anisotropy (Δ) on a powder-averaged spinon spectrum from the Schwinger boson theory. Top-left shows the INS data from E_i = 6 meV and T = 1.65 K (0.506 T_N). Other panels show Schwinger boson calculation results with different Δ and J_2 = 0. For the calculations, we used J_1 = 1.77 meV. Brown arrows on the right indicate positions twice the bandwidth of two-spinon bound states (1.6 meV), corresponding to the maximum energy of the two-magnon continuum (= pair creation of two-spinon bound states) anticipated from the $1/N^2$ order of Schwinger Boson theory, where N denotes the number of bosonic flavors.

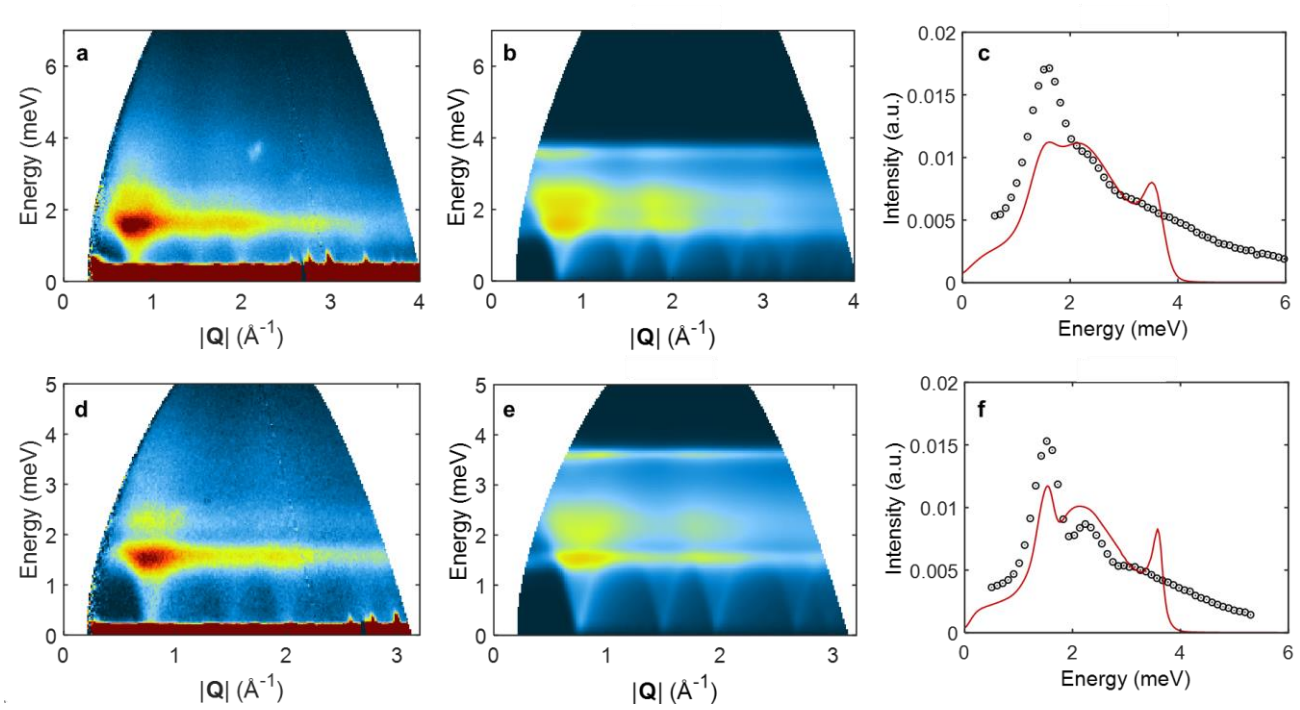

Supplementary Fig. 13 | Comparison between the INS data ($T < T_N$) and the Schwinger boson calculation with finite J_2. a, The INS data measured at 1.65 K with E_i = 10 meV and **b** the corresponding theoretical spectrum from parton Schwinger boson theory with J_1 = 1.87 meV, Δ = 0.54, and J_2 = 0.03. **c**, The intensity-energy plot of **a** (grey circles) and **b** (a solid red line) with the |**Q**| integration range set to [0.5, 1.5] Å^{-1}. **d**–**f,** Same as **a**–**c**, but from a different condition of incident neutron energy E_i = 6 meV. Note that larger J_1 is needed to match the observed excitation energy scale when finite J_2 is used (the optimal value of J_1 is 1.77 meV when J_2 = 0; see Fig. 4d in the main text). In **c** and **f**, error bars (= standard deviations) are much smaller than the data symbols.

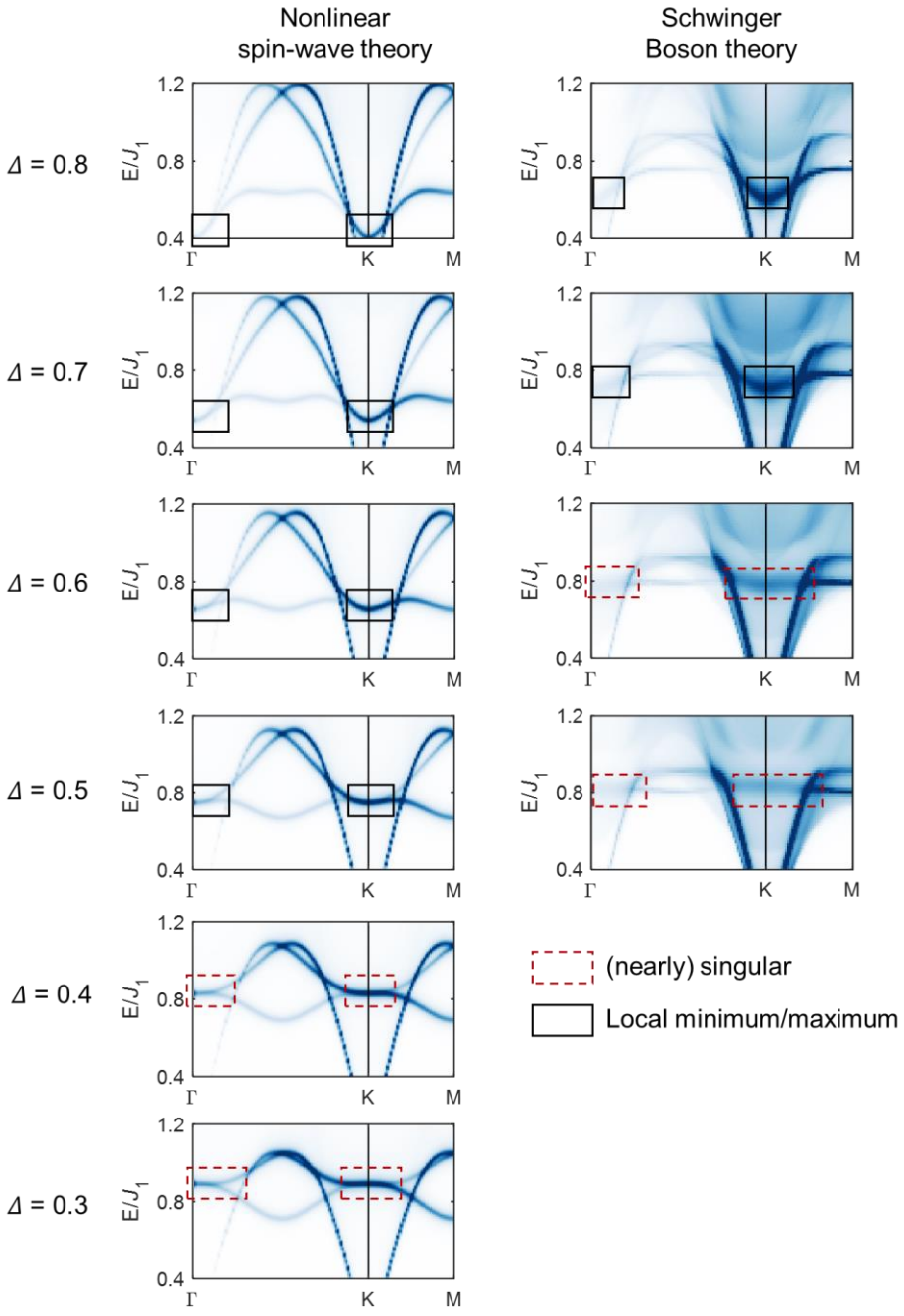

Supplementary Fig. 14 | Evolution of one-magnon dispersion along high-symmetry directions due to planar XXZ anisotropy. The calculation results in the first (second) column are from the NLSWT (Schwinger Boson) approach. The red dashed rectangles highlight the higher-order van-Hove singularity at the K and Γ points around the critical anisotropy Δ_0.

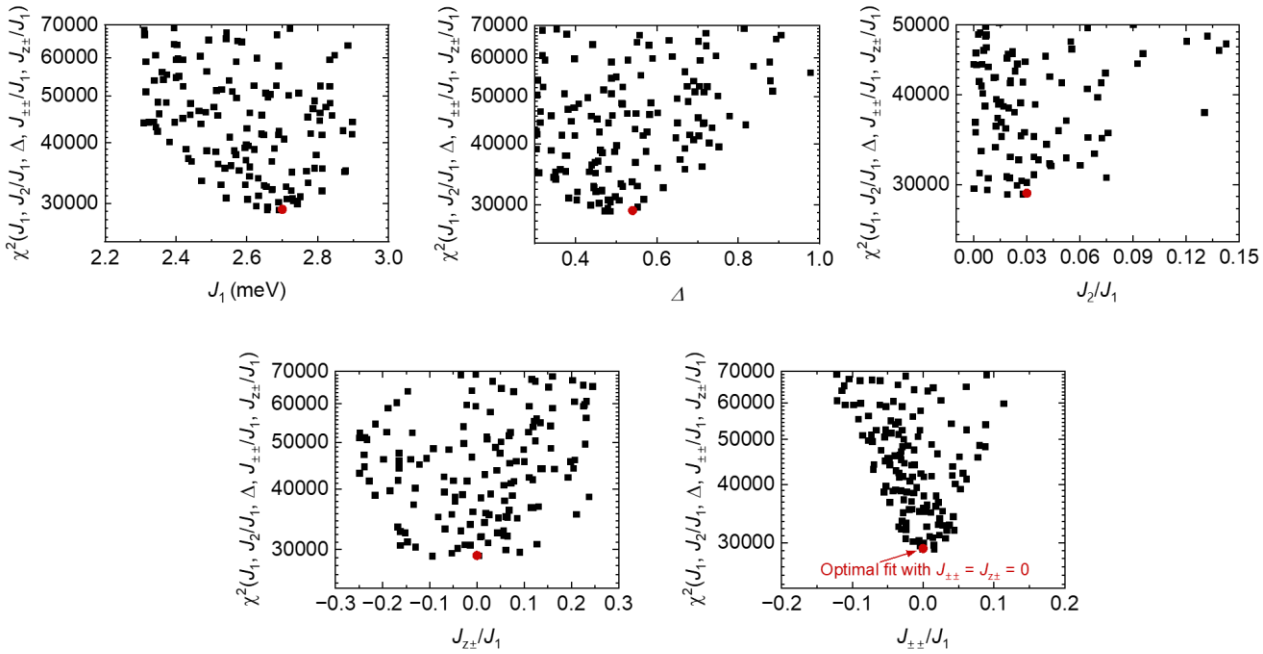

Supplementary Fig. 15 | Quantitative estimation of bond-dependent anisotropic exchange interactions ($J_{\pm\pm}$ and $J_{z\pm}$) using Bayesian optimization algorithm. Each panel shows the chi-square of the parameter sets sampled by the algorithm as a function of J_1, Δ, J_2/J_1, $J_{z\pm}/J_1$, and $J_{\pm\pm}/J_1$.

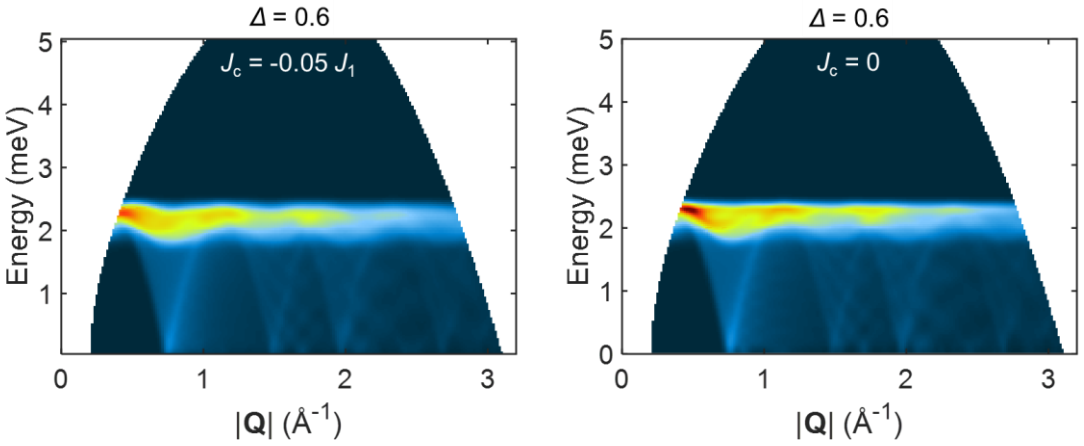

Supplementary Fig. 16 | A marginal effect of inter-layer coupling J_c in a powder-averaged excitation spectrum of BLCTO. The calculation was done by linear spin-wave theory with Δ = 0.60 and J_2 = 0.

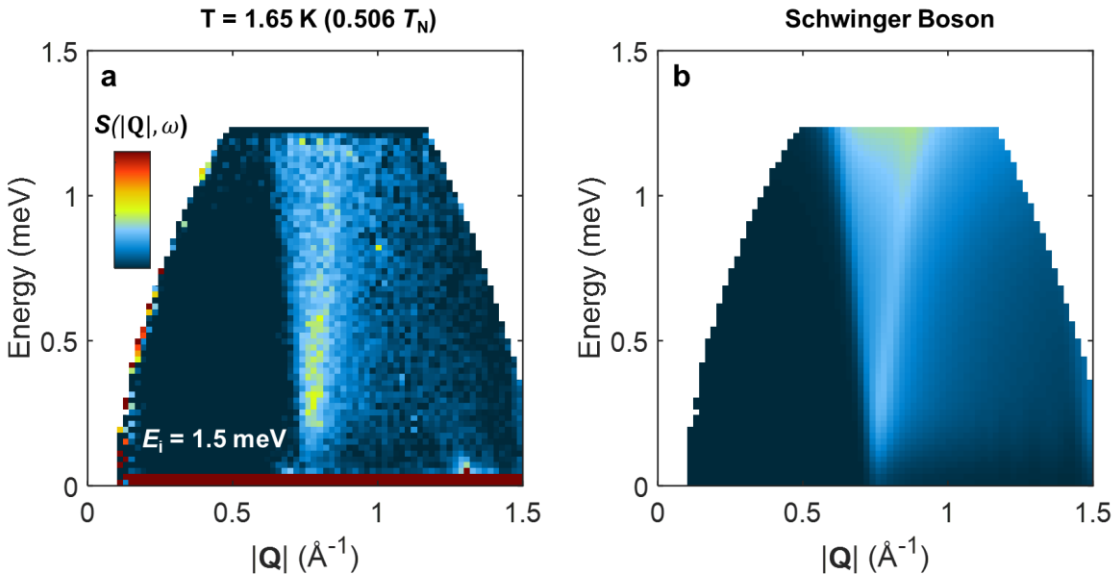

Supplementary Fig. 17 | A spin-wave spectrum of BLCTO in the sub-meV energy region. a, INS data measured with an incident energy E_i = 1.5 meV. **b**, Schwinger Boson calculation result with J_1 = 1.77 meV and Δ = 0.56 (i.e., no bond-dependent anisotropic exchange interactions). While the calculation should produce gapless magnon modes, the effects of powder averaging and resolution convolution can distort the gapless feature in the spectrum, as illustrated in **b**. A comparison between **a** and **b** implies no clear indication of an energy gap in BLCTO.

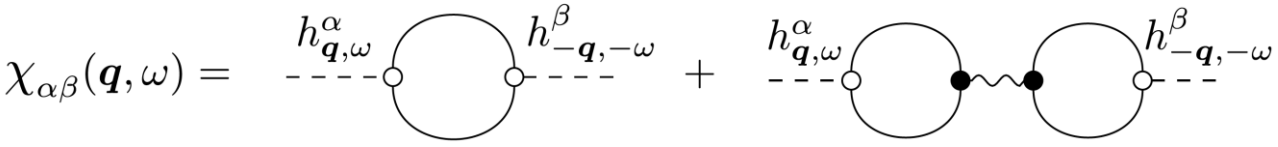

Supplementary Fig. 18 | The diagrammatic representation of the dynamical spin susceptibility in Eq. (14). On the righthand side (RHS), the first diagram corresponds to the saddle-point (SP) contribution, while the second term represents a Gaussian correction acting as a counter-diagram in the presence of a condensate. In the diagrams, dashed lines symbolize the external fields, and empty circles represent the external vertices. The solid lines denote the single-spinon propagator at the SP level, whereas the solid circles represent internal vertices. The wavy lines depict the propagator of the auxiliary fields, with their poles corresponding to the magnons of the theory.

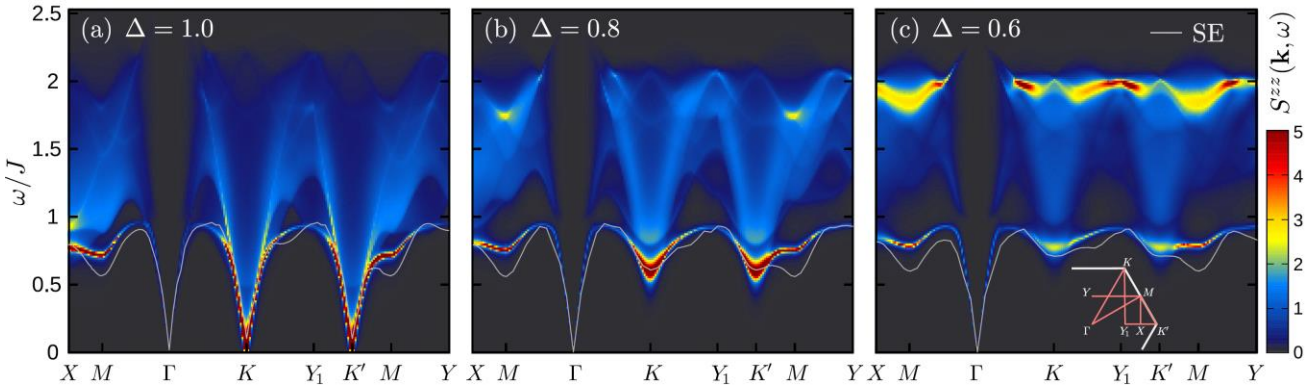

Supplementary Fig. 19 | Comparison of the S_{zz}(k, ω) of the SBT with the magnon dispersion of the Series Expansion calculation for different values of anisotropies. Panel (a) shows the isotropic case (Δ = 1) with ϵ_1 = 0.1, panel (b) shows the anisotropic case Δ = 0.8 with ϵ_1 = 0.122 and ϵ_2 = −0.35, and panel (c) shows the anisotropic case Δ = 0.6 with ϵ_1 = 0.15 and ϵ_2 = −0.35. The solid white line represents the SE magnon dispersion[20].

References

1 Liu, H., Chaloupka, J. & Khaliullin, G. Kitaev Spin Liquid in 3d Transition Metal Compounds. *Physical Review Letters* **125**, 047201 (2020).

2 Liu, H. & Khaliullin, G. Pseudospin exchange interactions in d7 cobalt compounds: Possible realization of the Kitaev model. *Physical Review B* **97**, 014407 (2018).

3 Yuan, B. *et al.* Dirac Magnons in a Honeycomb Lattice Quantum XY Magnet $CoTiO_3$. *Physical Review X* **10**, 011062 (2020).

4 Kojima, Y. *et al.* Quantum magnetic properties of the spin-1 2 triangular-lattice antiferromagnet $Ba_2La_2CoTe_2O_{12}$. *Physical Review B* **98**, 174406 (2018).

5 Kamiya, Y. *et al.* The nature of spin excitations in the one-third magnetization plateau phase of $Ba_3CoSb_2O_9$. *Nature communications* **9**, 2666 (2018).

6 Zhu, Z., Maksimov, P., White, S. R. & Chernyshev, A. Topography of spin liquids on a triangular lattice. *Physical review letters* **120**, 207203 (2018).

7 Maksimov, P. A., Zhu, Z., White, S. R. & Chernyshev, A. L. Anisotropic-Exchange Magnets on a Triangular Lattice: Spin Waves, Accidental Degeneracies, and Dual Spin Liquids. *Physical Review X* **9**, 021017 (2019).

8 Chaloupka, J., Jackeli, G. & Khaliullin, G. Kitaev-Heisenberg model on a honeycomb lattice: possible exotic phases in iridium oxides A_2IrO_3. *Physical review letters* **105**, 027204 (2010).

9 Sano, R., Kato, Y. & Motome, Y. Kitaev-Heisenberg Hamiltonian for high-spin d^7 Mott insulators. *Physical Review B* **97**, 014408 (2018).

10 Kim, C. *et al.* Bond-dependent anisotropy and magnon decay in cobalt-based Kitaev triangular antiferromagnet. *Nature Physics* **19**, 1624-1629 (2023).

11 Ghioldi, E. *et al.* Evidence of two-spinon bound states in the magnetic spectrum of $Ba_3CoSb_2O_9$. *Physical Review B* **106**, 064418 (2022).

12 Macdougal, D. *et al.* Avoided quasiparticle decay and enhanced excitation continuum in the spin-1 2 near-Heisenberg triangular antiferromagnet $Ba_3CoSb_2O_9$. *Physical Review B* **102**, 064421 (2020).

13 Brochu, E., Cora, V. M. & de Freitas, N. A Tutorial on Bayesian Optimization of Expensive Cost Functions, with Application to Active User Modeling and Hierarchical Reinforcement Learning. arXiv:1012.2599 (2010). <https://ui.adsabs.harvard.edu/abs/2010arXiv1012.2599B>.

14 Pedregosa, F. *et al.* Scikit-learn: Machine learning in Python. *the Journal of machine Learning research* **12**, 2825-2830 (2011).

15 Matin, S. An opinionated Julia wrapper for Bayesian Optimization. Available online: https://github.com/sakibmatin/BayesOptim.jl.

16 Scheie, A. O. *et al.* Proximate spin liquid and fractionalization in the triangular antiferromagnet $KYbSe_2$. *Nature Physics* **20**, 74-81 (2023).

17 Zhang, S.-S., Ghioldi, E., Manuel, L., Trumper, A. & Batista, C. D. Schwinger boson theory of ordered magnets. *Physical Review B* **105**, 224404 (2022).

18 Zhang, S.-S. *et al.* Large-S limit of the large-N theory for the triangular antiferromagnet. *Physical Review B* **100**, 104431 (2019).

19 Trumper, A., Manuel, L., Gazza, C. & Ceccatto, H. Schwinger-boson approach to quantum spin systems: Gaussian fluctuations in the "natural" gauge. *Physical review letters* **78**, 2216 (1997).

20 Ghioldi, E. A. *et al.* Magnons and excitation continuum in XXZ triangular antiferromagnetic model: Application to $Ba_3CoSb_2O_9$. *Physical Review B* **91**, 134423 (2015).

21 Oitmaa, J. Magnetic phases in the J1− J2 Heisenberg antiferromagnet on the triangular lattice. *Physical Review B* **101**, 214422 (2020).

22 Zheng, W., Fjærestad, J. O., Singh, R. R., McKenzie, R. H. & Coldea, R. Excitation spectra of the spin-1/2 triangular-lattice Heisenberg antiferromagnet. *Physical Review B* **74**, 224420 (2006).

23 Arovas, D. P. & Auerbach, A. Functional integral theories of low-dimensional quantum Heisenberg models. *Physical Review B* **38**, 316 (1988).

24 Auerbach, A. *Interacting electrons and quantum magnetism*. (Springer Science & Business Media, 1998).

25 Ghioldi, E. A. *et al.* Dynamical structure factor of the triangular antiferromagnet: Schwinger boson theory beyond mean field. *Physical Review B* **98**, 184403 (2018).

26 Zhu, Z., Maksimov, P., White, S. R. & Chernyshev, A. Disorder-induced mimicry of a spin liquid in $YbMgGaO_4$. *Physical review letters* **119**, 157201 (2017).

27 Quirion, G. *et al.* Magnetic phase diagram of $Ba_3CoSb_2O_9$ as determined by ultrasound velocity measurements. *Physical Review B* **92**, 014414 (2015).

28 Wildes, A. R., Simonet, V., Ressouche, E., Ballou, R. & McIntyre, G. J. The magnetic properties and structure of the quasi-two-dimensional antiferromagnet $CoPS_3$. *Journal of Physics: Condensed Matter* **29**, 455801 (2017).

29 Kim, C. *et al.* Spin waves in the two-dimensional honeycomb lattice XXZ-type van der Waals antiferromagnet $CoPS_3$. *Physical Review B* **102**, 184429 (2020).

30 Sheng, J. *et al.* Two-dimensional quantum universality in the spin-1/2 triangular-lattice quantum antiferromagnet $Na_2BaCo(PO_4)_2$. *Proceedings of the National Academy of Sciences* **119**, e2211193119 (2022).

31 Zhong, R., Guo, S., Xu, G., Xu, Z. & Cava, R. J. Strong quantum fluctuations in a quantum spin liquid candidate with a Co-based triangular lattice. *Proceedings of the National Academy of Sciences* **116**, 14505-14510 (2019).

32 Doi, Y., Hinatsu, Y. & Ohoyama, K. Structural and magnetic properties of pseudo-two-dimensional triangular antiferromagnets $Ba_3MSb_2O_9$(M = Mn, Co, and Ni). *Journal of Physics: Condensed Matter* **16**, 8923-8935 (2004).

33 Jiao, J. *et al.* Quantum Effect on the Ground State of the Triple-Perovskite $Ba_3MNb_2O_9$ (M= Co, Ni, and Mn) with Triangular-Lattice. *Chemistry of Materials* **34**, 6617-6625 (2022).

34 Ivanov, S., Nordblad, P., Mathieu, R., Tellgren, R. & Ritter, C. Neutron diffraction studies and the magnetism of an ordered perovskite: Ba_2CoTeO_6. *Dalton Transactions* **39**, 5490-5499 (2010).

35 Kojima, Y., Kurita, N., Tanaka, H. & Nakajima, K. Magnons and spinons in Ba_2CoTeO_6: A composite system of isolated spin-1/2 triangular Heisenberg-like and frustrated honeycomb Ising-like antiferromagnets. *Physical Review B* **105**, L020408 (2022).

36 Paddison, J. A. M. Spinteract: a program to refine magnetic interactions to diffuse scattering data. *Journal of Physics: Condensed Matter* **35**, 495802 (2023).